Investigation of the magnetic and electrochemical properties of A-site double-doping $La_{0.7}Sr_xMg_{0.3-x}FeO_3$ Perovskite

S. SASEETHA[1,*], M. NAGARAJAN[1], S. SUBHA[1], S. C. VELLA DURAI[2], K. ANITHA RANI[3]
[1]*Research Department of Physics, V.O.Chidambaram College, Thoothukudi – 628008, Tamilnadu, India*
[2]*PG and Research Department of Physics, Sri Paramakalyani College, Alwarkurichi, Tenkasi-627412, Tamilnadu, India*
[3]*Department of Physics, SSDM College, Kovilpatti-628501, Tamilnadu, India (Affiliated to Manonmanium Sundaranar University,Tirunelveli – 627018, Tamilnadu, India*

The sol-gel citrate auto-combustion process was used for obtaining polycrystalline nano compounds of $La_{0.7}Sr_xMg_{0.3-x}FeO_3$ that included varying quantities of Sr(x = 0.00, 0.01, 0.15, and 0.20) nanopowders. Thermo gravimetric analysis (TGA), X-ray diffraction (XRD), scanning electron microscopy (SEM) with energy dispersive spectroscopy (EDS), Fourier transform infrared spectroscopy (FT-IR), and UV-vis spectro photometry (UV-vis) were used to analyse these as-prepared particles. A vibrating sample magnetometer (VSM) was used to examine the nanomagnetic characteristics. Using CV, GCD, and EIS, the electrochemical characteristics were studied. The diameters of nanoparticle crystallites are determined to be between 21 and 28 nm, and they vary with increasing Sr and Mg concentrations. All samples have an orthorhombic structure with a Pnma (62) space group, according to XRD analysis. In accordance to the FT-IR spectra, the O-Fe-O metal oxygen bonds are present in the FeO_6 octahedra. From the UV-vis spectra, the optical band gaps are discovered to be in the range of 2.08 to 2.13 eV. SEM images were used to examine the microstructure and surface morphology. Whereas the M-H loop of the doped samples tends to be weak ferromagnetic with increasing Sr concentration, which of the pure sample is paramagnetic. The Sr and Mg-doped material with x = 0.2 has increased magnetization, remanent magnetization, and coercive field to 0.4 emu/g, 0.14 emu/g, and 185 Oe respectively. In comparison to non-doped and double-doped LF samples, $La_{0.7}$ $Sr_xMg_{0.3-x}FeO_3$ (x=0.2) has a greater specific capacitance of 379 F/g at 10 mV/s.

(Received December 4, 2023; accepted July 30, 2024)

Keywords: Electrochemical, Magnetic, Polycrystalline, Perovskite, Specific capacitance

1. Introduction

Ferrite materials are unique in nature because they have distinct properties such as higher permeability, lower dielectric loss, high resistivity, moderate magnetization, and so on, making them ideal for a variety of applications. Over the past few decades, researchers have studied color photography, ferrofluids, high-frequency devices and fast mail, etc. They continued to develop electronic, magnetic and ferrite materials for applications [1, 2]. Many studies have recently been conducted in order to develop new nano-ferrite materials for applications such as electrode material for Li-ion batteries [3], the production of bio-diesel [4], gas sensors [5], nano-catalysts [6], super-capacitors [7], electrical [8] etc. Among many ferrites, ABO_3 perovskite oxides have attracted more attention in the fields of gas sensors [9], environmental protection [10, 11], solar energy utilization [12, 13], industrial catalysis [14, 15], and photo catalysis [16] due to their stable crystal structure, excellent catalytic activities, and unique electromagnetic properties. When the A and B positions are changed by replacing metal ions with similar radii, the structure of the nanocrystal remains unchanged. [17]. One of the ABO_3 perovskites is lanthanum ferrites ($LaFeO_3$), which has promising applications in the fields of sensing [18, 19], magnetism [20, 21], and electricity [22, 23]. The $LaFeO_3$ crystal has an orthorhombic structure; the six oxygen ions that surround the Fe3+ ions in $LAFeO_3$ form an octahedron [24]. The features of pure and doped $LaFeO_3$ depend on their structure, size, phase, and morphology, and all of which are significantly connected to the preparation process. The sol gel process has emerged as one of the most effective techniques, making it the perfect way for producing $LaFeO_3$ perovskite that has remarkable purity, narrow particle size distribution, controlled stoichiometry and morphology [25, 26]. $LaFeO_3$ is a research hotspot because of its superior catalytic, electromagnetic and gas-sensing capability. Based on the information mentioned previously, the purpose of this work is to investigate the effects of strontium and magnesium doping on the A-site, which means lanthanum is present at that site. The optical, structural, morphological, and electrical characteristics of pure $LaFeO_3$ and the doping material were prepared using the sol-gel citrate auto combustion technique.

2. Experimental

2.1. Materials and methods

Using the sol-gel process using metal nitrates as precursors (x = 0.00, 0.10, 0.15, and 0.20), $La_{0.7}$ $Sr_xMg_{0.3-x}FeO_3$ samples were produced. Analytical-grade chemicals were employed throughout without further purification. $La(NO_3)_3.6H_2O$ was initially dissolved in distilled water in a stoichiometric ratio with the addition of $Sr(NO_3)_2$,

$Mg(NO_3)_2$, and $Fe(NO_3)_3.9H_2O$. The aforementioned compounds were from Sigma Aldrich with a purity of 99%. The mixture was then given a last addition of citric acid for the combustion process. The mixture needed to be thoroughly stirred and heated up to 80 °C for around five hours until a metal nitrate gel was obtained. When the temperature was increased slightly, about 120^0 °C, the auto combustion took place, and the burnt ash was prepared. The powder sample was prepared by drying the ash, grinding it in an agate mortar, and heating it at 200°C for 12 hours. The resulting product is pulverized again and then sintered at 700°C for 5 hours to form the final product. $LaFeO_3$, $La_{0.7}Sr_{0.1}Mg_{0.2}FeO_3$, $La_{0.7}Sr_{0.15}Mg_{0.15}FeO_3$, and $La_{0.7}Sr_{0.2}Mg_{0.1}FeO_3$ were the final products. The samples mentioned above were then identified as LF, 1LSMF, 2LSMF, and 3LSMF.

2.2. Working electrode (WE) preparation

In conventional electrochemical experiments like cyclic voltammetry, the three electrodes represent a working electrode, a counter electrode, and a reference electrode, respectively. The reference electrode has been employed to accurately measure the applied potential in relation to a steady reference response as current flows between the counter and working electrodes. A reference electrode has an equilibrium potential that is well defined and stable. It serves as a reference point for determining the potential of the other electrodes in an electrochemical cell. The saturated calomel electrode (SCE), the standard hydrogen electrode (SHE), and the AgCl/Ag electrode are a few examples of reference electrodes that are frequently used. In order to complete the electrical circuit, the counter electrode is required. The movement of electrons between the WE and CE is measured as current. The most common counter electrodes are platinum wire or disc; even carbon-based electrodes are also used [27]. Three drops of N-methyl-2-pyrrolidone (NMP, C5H9NO) solvent were added to the weight proportion of the active material (which constitutes eighty percent of the LSMF sample), 15% carbon black, and 5% PVDF (polyvinylidene fluoride) binder used to produce the working electrodes (WE). The obtained homogeneous 80 mg slurry was then applied to a nickel foam patch of 1 cm^2 and allowed to dry for 20 hours at a temperature of 100°C in the oven. Utilizing a three-electrode setup with an obtained LSMF working electrode, a counter electrode (platinum wire), a reference electrode (Ag-AgCl), and 3 M KOH as an electrolyte in ambient conditions, the super capacitive behaviour of the LSMF materials has been investigated.

3. Result and discussion

3.1. Thermal analysis

The initial dryness of the samples took place at a low temperature of roughly 50–100 °C, releasing molecules of water. As the samples had enough kinetic energy to free the bonded water molecules, they initially absorbed heat from the environment, and the minimum amount of weight loss was seen in the TGA curve (Fig. 1(a)). The peak of the breakdown occurred at temperatures ranging from 100 to 400 ^{0} C. Significant liberation of bridging oxygen resulted from the considerable weight loss that was seen in the TGA profile. The remaining materials elements were completely oxidized at the higher temperature, about 500^0 C, and at the same time that the LSMF ($La_{0.7}$ $Sr_xMg_{0.3-x}FeO_3$ (x = 0.00, 0.10, 0.15, and 0.20)) compound was also formed, which produced a significant exothermic peak in the DTA profile (Fig. 1(b)). The TGA trace for all four compounds did not significantly change with temperature up to 700^0 C, indicating that a thermodynamically stable crystalline phase composition state had been attained [28, 29].

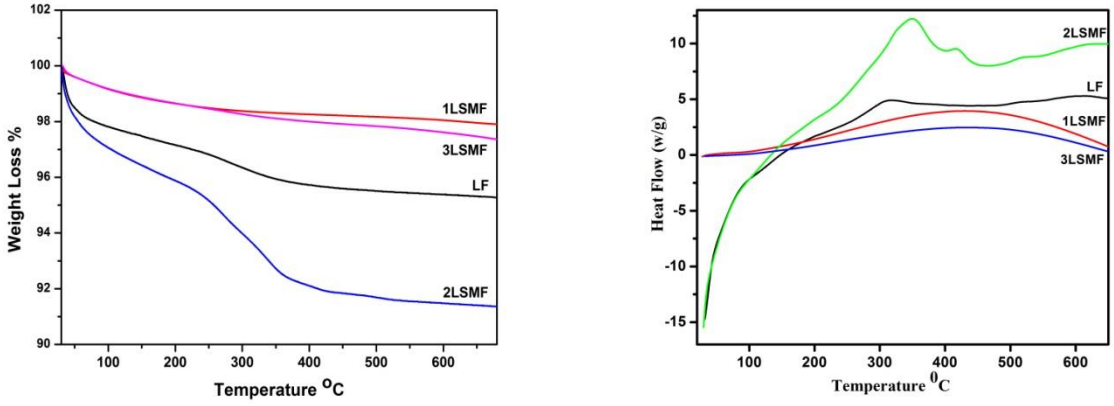

(a) *(b)*

Fig. 1. (a) TGA analysis of LF and LSMF samples; (b) DTA analysis of LF and LSMF samples (color online)

3.2. FTIR analysis

The Fe-O band in the perovskite LaFeO3 is seen for all four samples (Fig. 2) as a strong band at 570 cm^{-1}. The formation of this perovskite phase in these four samples is confirmed by the presence of this cluster. The FT-IR spectra of the samples from the pre-LF, 1LSMF, 2LSMF, and 3LSMF ($La_{0.7}$ $Sr_xMg_{0.3-x}FeO_3$ (x = 0.10, 0.15, and 0.20) are displayed in Fig. 2. The synthesised particles, which have transmission ranges of 400–4000 cm^{-1}, showed multiple

transmissions. It has been determined that the H-O-H band from the moisture is responsible for the transmission bands that are around 1600 cm^{-1} [30]. Fe-O stretching and O-Fe-O deformation vibrations have been associated with strong peaks at 570 and 410 cm^{-1}, respectively [31, 32]. These bands result from the octahedral BO6 (FeO6) stretching modes of the perovskite structure ABO_3. A symmetric stretching vibration (ν1) at 1110 cm^{-1} shows the mode of carbonate, the result coincides with that of a previous study [33].

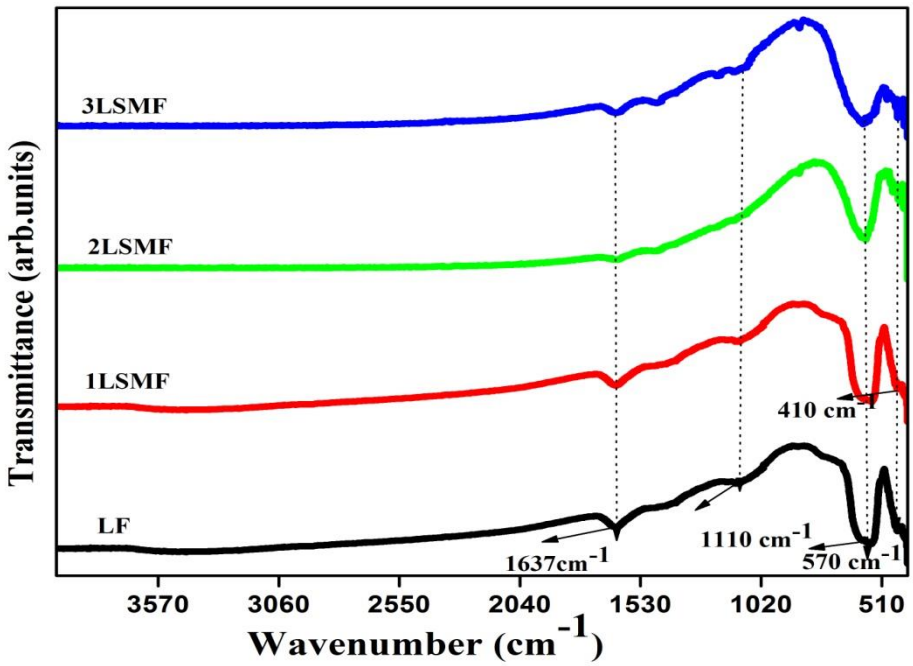

Fig. 2. FTIR pattern of LF and LSMF samples (color online)

3.3. XRD analysis

Fig. 3 (a) indicates the X-ray diffraction patterns for the LSMF ($La_{0.7}$ $Sr_xMg_{0.3-x}FeO_3$ (x = 0.10, 0.15, and 0.20) powders after five hours of heating at 700 °C. X'Pert High Score Plus software was used to analyse the XRD pattern. Finding the appropriate space group and the perovskite phase's lattice parameters were the objectives. The absolute and relative maximum intensities of the reflections, as well as the peak locations, were determined in the first stage. A comparison between the experimental diffractograph and the ICDD (International Centre for Diffraction Data) reference base information was then made. Without any discernible secondary phases, the XRD pattern reveals a perovskite structure that has been well-crystallised. Fig. 3's diffraction peaks all closely matched the ICDD PDF (37–1493). Indexation of the reflections and lattice parameter determination followed next.

According to the results, the A-site Sr^{2+} and Mg^{2+} substituted lanthanum ferrite crystallised into an orthorhombic unit cell having the Pbnm space group Pn.a-(62) with the cell's parameters a = 5.5669Å, b = 7.854Å, and c = 5.5530Å. The pattern produced by XRD exhibits sharp peaks that correspond to the planes (1 0 1), (1 2 1), (2 2 0), (2 0 2), (2 4 0), (2 4 2), and (2 0 4). The LF, 1LSFM, 2LSFM, and 3LSFM have average crystallite sizes of 27 nm, 24 nm, 21 nm, and 26 nm, respectively. Using Scherer's equation 1, crystalline size was calculated using the full width half maximum (FWHM) of the peak [34].

$$D = 0.9\lambda/\beta cos\theta \quad (1)$$

where D is the crystallite size in nm, β is the full width at half maximum (FWHM), λ is the wavelength of the X-rays (1.5406 Å), and θ is the diffraction peak angle. Fig. 3 (b) indicates the crystalline size was varied with respect to different concentration.

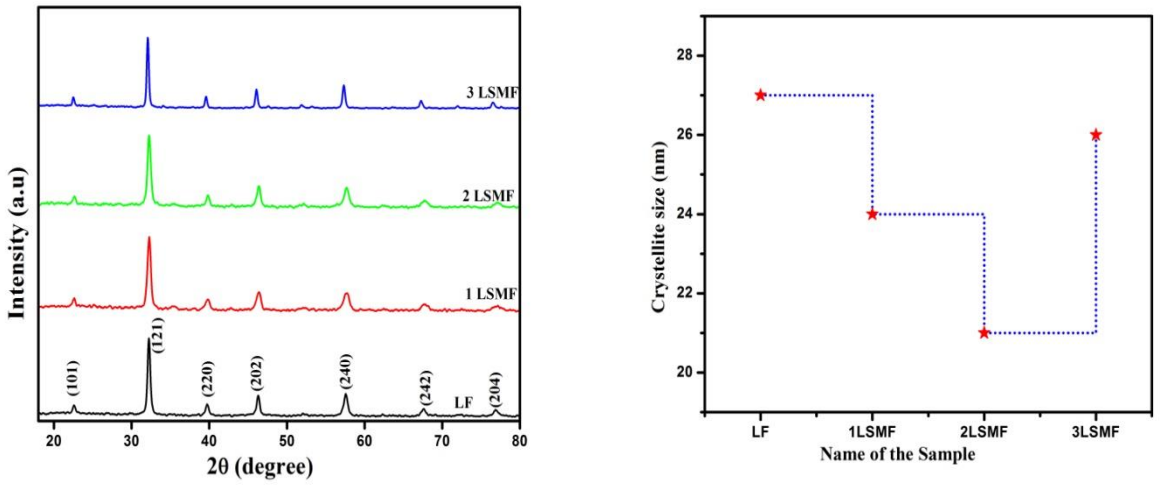

(a) *(b)*

Fig. 3. (a) X-ray diffraction pattern of LF and LSMF samples; (b) Comparison of crystallite size of the samples (color online)

3.4. UV-Vis analysis

In order to describe the optical characteristics of the LF and LSMF ($La_{0.7}$ $Sr_xMg_{0.3-x}FeO_3$ (x = 0.10, 0.15, and 0.20) nanoparticles, UV-visible spectroscopy is used. For example, for direct transformation, this is achieved by extending the line outside the curve until the absorbance is zero. (Fig. 4 (a) and (b)). All samples had direct band gaps that are estimated in a range of approximately 2.08 eV, 2.10 eV, 2.13 eV, and 2.08 eV. These findings agree with the previously published value of 2.1 eV for LaFeO3 nanoparticles synthesized using the sol-gel auto-combustion technique [35-37]. It has been discovered that when Sr and Mg concentrations increase, the optical band gaps do not change appreciably.

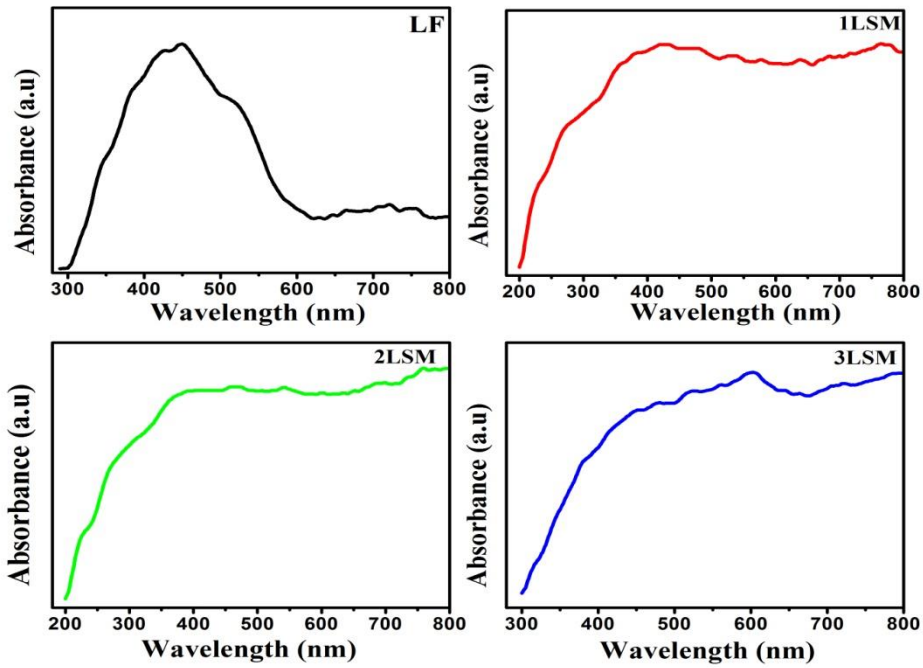

(a)

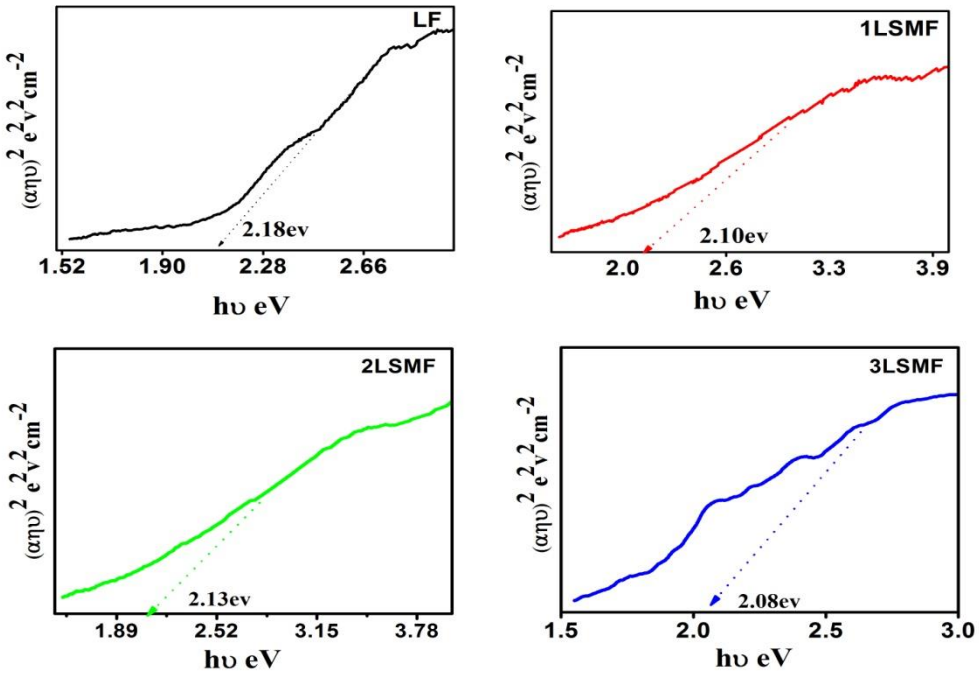

(b)

Fig. 4. (a) UV absorption plot; (b) Tauc plot (color online)

3.5. Morphological analysis (SEM with EDAX)

The morphological analysis of the obtained $La_{0.7}Sr_xMg_{0.3-x}FeO_3$ (x = 0.0, 0.10, 0.15, and 0.20) nanoparticles were examined by the scanning electron microscopy (SEM) and are shown in Fig. 5 (a to d). SEM images of $La_{0.7}Sr_xMg_{0.3-x}FeO_3$ (x = 0.10, 0.15, and 0.20) samples shown in Fig. 5 (b, c and d) reveals that all the samples exhibit a arrangement of homogeneous agglomerated nanoparticles with coral like porous microstructure with non-spherical shape. Fig. 5 (a) shows the presence of pure $LaFeO_3$ nanoparticles, which are homogeneous and agglomerated Nanoparticles with clustered cylindrical grains.

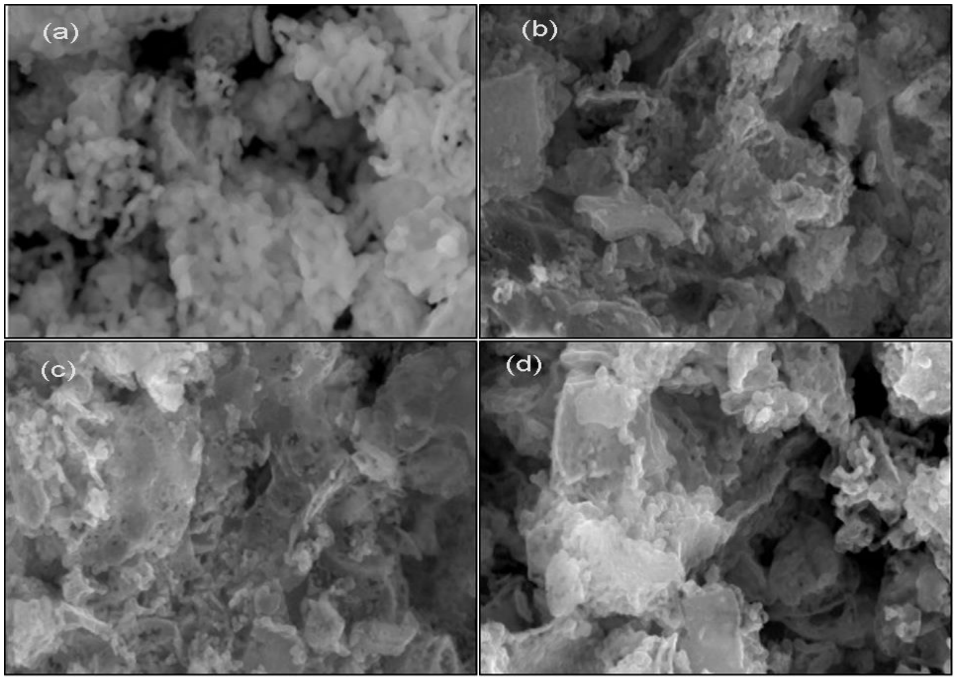

Fig. 5. SEM images of LF and LSMF samples

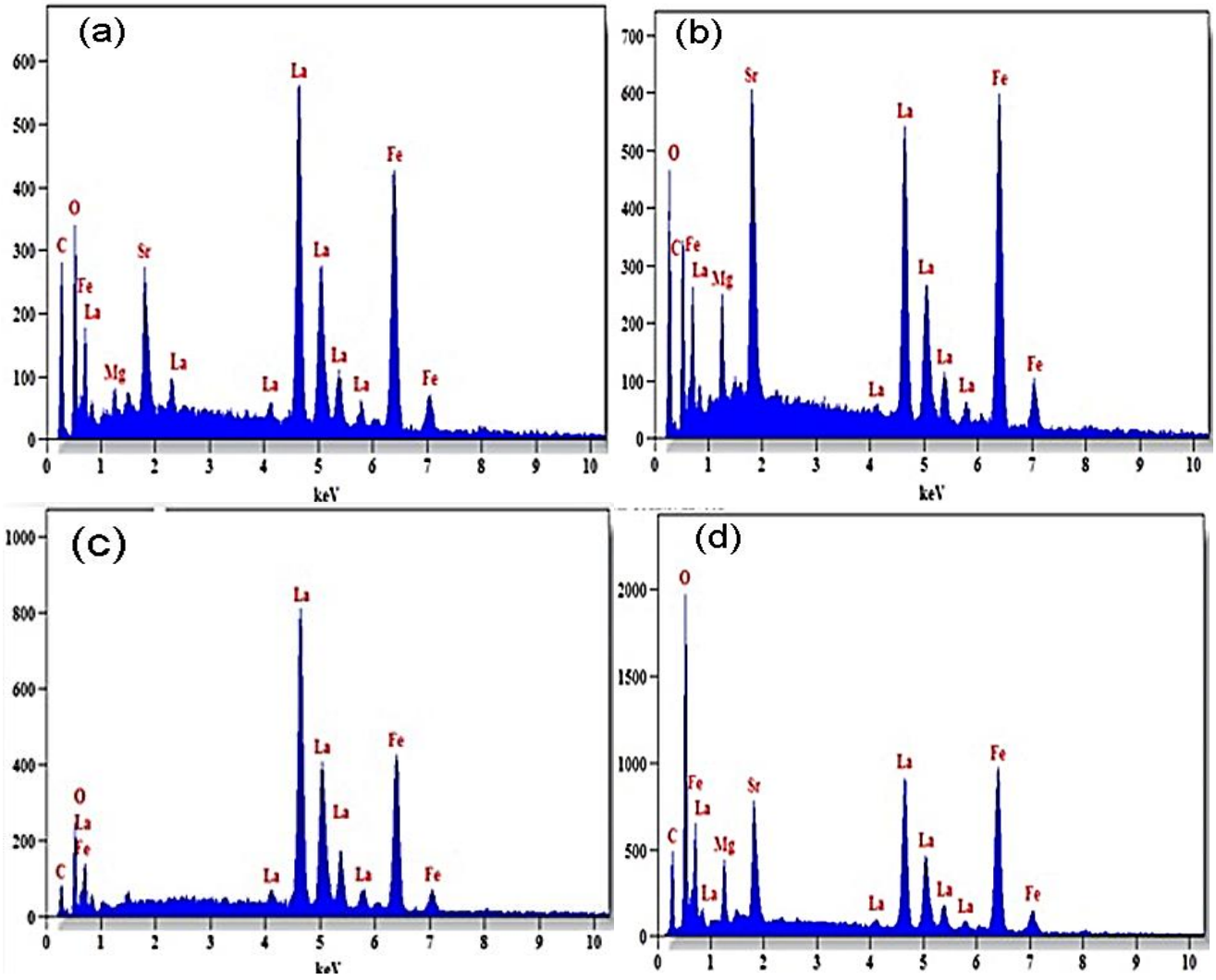

Fig. 6. EDAX images of LF and LSMF samples (color online)

Nano particles are agglomerated due to the presence of magnetic interactions among the particles [38]. EDAX spectra of pristine and Sr^{2+} & Mg^{2+}-doped Lanthanum ferrites, $La_{0.7}$ $Sr_xMg_{0.3-x}FeO_3$ (x = 0.0, 0.1, 0.15, and 0.2), are shown in Fig. 6(a to d). Fig. 6a shows the peaks of La, Fe, and O elements in pure $LaFeO_3$, and Fig. 6(b to d) shows the peaks of La Fe, Sr, Mg, and O elements for Sr and Mg-doped $LaFeO_3$ samples. It's interesting to notice that the preparation parameters entirely encourage the development of mixed ferrites and enable us examine how adding more Mg and Sr affects the lanthanum ferrite's physical characteristics. The aforementioned findings demonstrate that the pristine LF, Sr, and Mg-doped $LaFeO_3$ phases may occur.

3.6. VSM analysis

Fig. 7 (a to d) displays the findings from a measurement made using a Vibrating Sample Magnetometer (VSM)-250 on pure $LaFeO_3$ and $La_{0.7}Sr_x$ $Mg_{0.3-x}$ FeO_3 samples that were sintered at a high temperature of 700°C. The M-H curve, which almost coincides with the axis of H and seems to be a straight line, indicates that the sample shows paramagnetic characteristics for X = 0.0(LF). $LaFeO_3$ becomes a weak ferromagnetic material when Sr and Mg are incorporated as dopants. It can be observed in Fig. 7 (a), the synthesis of $LaFeO_3$ with a higher dopant concentration results in more ferromagnetic characteristics. The photograph indicates clearly that the samples reveal some well-formed hysteresis loops, which provide proof to their weak ferromagetic nature. The samples' increased saturation (Ms) and magnetic remanence (Mr) are indicators as well. The sample's magnetic parameters at x = 0.1 are 0.0085 emu/g of magnetic saturation (Ms), 0.205 emu/g of remanence (Mr), and 115 Oe of coercivity (Hc). At x = 0.2, the sample's (3LSM) Ms, Mr, and Hc are 0.04 emu/g, 0.014 emu/g, and 185 Oe [40] respectively. The nanoparticles are uniaxially anisotropic single-domain materials if the theoretical squareness (Mr/Ms) is less than 0.5, according to the Stoner Wolfarth results. Outstanding hysteresis loops and low coercivity in the sample suggest that it may be readily demagnetized and might make an outstanding electromagnet material.

The magnetization increases as the dopant of Sr^{2+} increases and also the coercivity of the sample increases gradually as the Sr^{2+} ion concentration is gradually raised.

The following values 0.24emu/g, 0.28emu/g, and 0.30emu/g were the estimated squareness of the samples 1LSMF, 2LSMF, and 3LSMF, respectively. All the parameters were shown in the Table 1. The ionic radii of La^{3+}, Sr^{2+}, and Mg^{2+} ions are 0.136 nm, 0.113nm, and 0.072 nm, respectively. When we compared the ionic radii of Sr^{2+} and Mg^{2+} ions with La^{3+}, the Mg^{2+} is much smaller than the ionic radii of La^{3+} ions. When Sr^{2+} and Mg^{2+} ions replace La^{3+}, the bond length is reduced and the super exchange angle between Fe^{3+} and O_2 is increased. This strengthens the super exchange interaction and increases the magnetization of doped $LaFeO_3$. [40, 41].

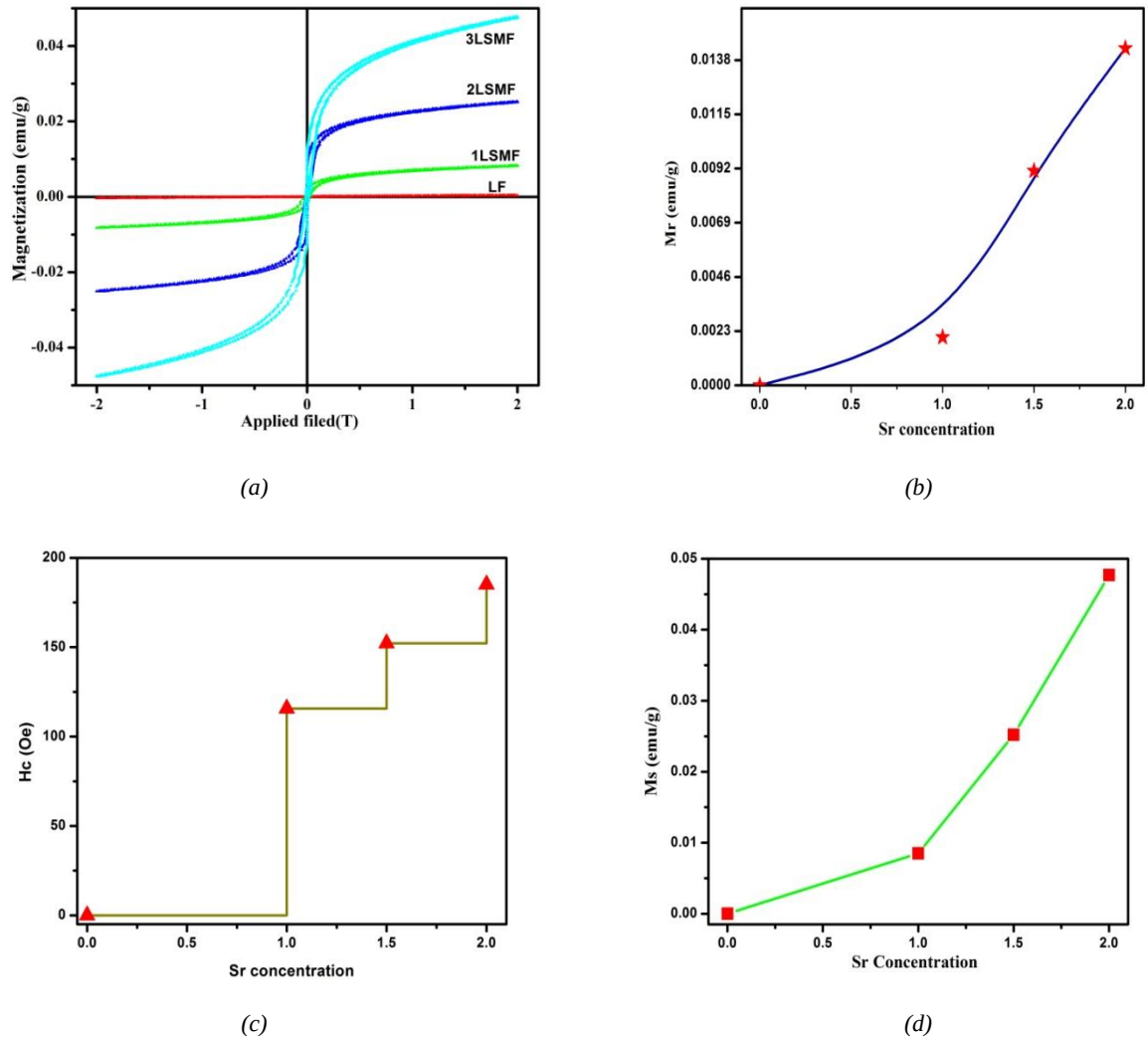

(a) *(b)*

(c) *(d)*

Fig. 7. VSM analysis plots (color online)

Table. 1. M_r, M_s, R and H_c of samples with various Sr concentration

Concentation of Sr	Mr (emu/g)	Ms(emu/g)	R=Mr/Ms	Hc(Oe)
1.0	0.002	0.008	0.25	115
1.5	0.007	0.025	0.28	152
2.0	0.014	0.047	0.30	185

3.7. Electrochemical analysis

The best techniques for examining the electrochemical behavior of electrode materials are CV and GCD. In the current work, CV and GCD measurements were carried out in a three-electrode system, which contained an Ag/AgCl as a reference electrode and graphite plate as a counter electrode in a 3 M KOH electrolyte. In order to investigate the supercapacitance efficiency of the synthesised powdered substances (pristine LF, 1LSMF, 2LSMF, and 3LSMF), the following equation could be used for estimating the specific capacitance (Cs) of the samples employed in the working electrodes based on the CV data:

$$C_p = \frac{\int I \Delta V}{vm\Delta V} \quad (2)$$

Here, I stand for current density (A), V for the potential window, for scan rate (V/s), and m for the mass of electro active material adhered to the counter electrode [42]. Fig. 8 (a) illustrates the CV curves of the LF, 1LSMF, 2LSMF, and 3LSMF nanocomposite materials at 10 mV Scan rate. Some significant reduction and oxidation peaks may be seen on all CV curves. The deflection in capacitor behaviour demonstrates the existence of a Faradic reversible redox reaction pertinent to surface functions [43]. Additionally, the existence of oxidation reduction peaks suggests that lanthanum ferrite materials behave in a pseudocapacitance manner [44]. These findings are quite consistent with prior research on oxide and ferrite nanomaterials [45]. In comparison to pure LF, all of the LSMF samples (A-site comprising Sr and Mg) generally revealed enhanced supercapacitor behaviour with higher capacitance and a larger potential window. A-site element doping is more likely to affect the morphology of perovskite structures, since it can alter crystallite size and result in lattice deformation. This therefore affects the link between metal and oxygen; this may have an effect on oxygen vacancies. A significant oxidation peak can be seen at 0.5 V and a considerable redox peak can be seen at 0.2 V when an A-site is doped by 30% Sr and Mg. The larger Cp, which was roughly 379 F/g at 10 mV/s for the 3LSMF sample and 233 F/g for non-doped lanthanum ferrite, is the cause of the CV curve's wide area (Fig. 8 (b)). Adding Sr and Mg to ferrite samples enhances their electrochemical behaviours, resulting in ferrite samples with larger potential windows. In general, treating ABO_3 perovskite nanostructures with various dopants leads to lattice deformation in the structure, resulting in a significant impact on the concentration of oxygen vacancies and the electrochemical properties.

The 3LSMF sample's CV curves are displayed in Fig. 8 (c) at various scan rates of 10, 20, 30, 40, 50, 60, 70, 80, 90, and 100mV/s. It is clear that the overall peak current density of the 3LSMF consistently grew with greater potential scan rates, in contrast to reduction peaks with higher potential scan rates, where the peak moved towards lower potential. The peaks' position is shifted toward both ends while the loop area is larger due to the polarization effect and internal diffusion resistance in the electrode [46]. Fig. 8 (c), depicts the typical CV curve of lanthanum ferrite with A-site Sr and Mg dopants $La_{0.7}$ $Sr_xMg_{0.3-x}FeO_3$(x=0.2) in the stable potential window of 0.0 to 0.7V at a scan rate of (10, 20, 30, 40….100mV/s).

Electrochemical impedance spectroscopy (EIS) study further supported the enhanced electrochemical performance of the 3LSMF nanocomposite sample. The Nyquist plot and equivalent circuit of the EIS spectra for the LF, 1LSMF, 2LSMF, and 3LSMF samples is displayed in Fig. 8 (d) and inset figure. Nyquist plot typically includes three sections, the x-intercept at the beginning of the curve regarded as effective series resistance (ESR), which is the first component in the higher frequency area. As can be observed, the ESR values for all three samples are lower (1.0) and quite similar to one another. The second section is a semicircle that is supposed to have a charged transfer resistance (R_{ct}) equal to its diameter in the mid-frequency zone. The graphic demonstrates that for samples 2LSMF and 3LSMF, there is no discernible semi-circle zone, indicating that a minimal R_{ct} may be taken into consideration for the samples. The vertical spike in the low frequency region, which is thought to reflect Warburg resistance (Z_w) to ionic transport at the electrode/electrolyte interface, makes up the third portion. The vertical line of an ideal capacitor is about 90 degrees parallel to the fictitious axis of the EIS diagram. In accordance with this explanation, the 2 LSMF and 3 LSMF samples displayed a nearly vertical line in the lower frequency range, demonstrating the predicted capacitive behaviour [47, 48]. The lowest R_s and R_{ct} are produced when the appropriate proportions of A-dope substances are used, which increases the specific capacitance of perovskite materials [49].

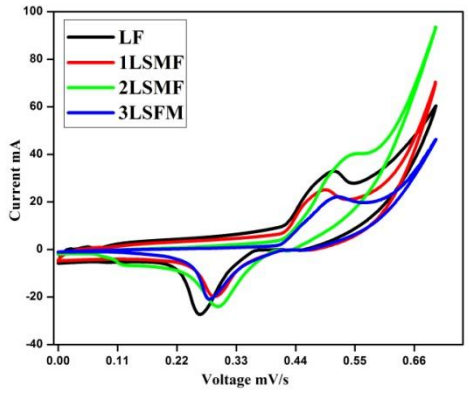

(a)

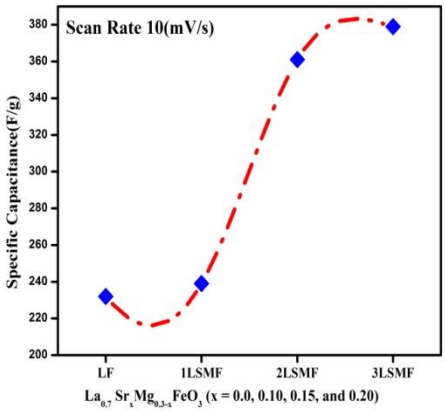

(b)

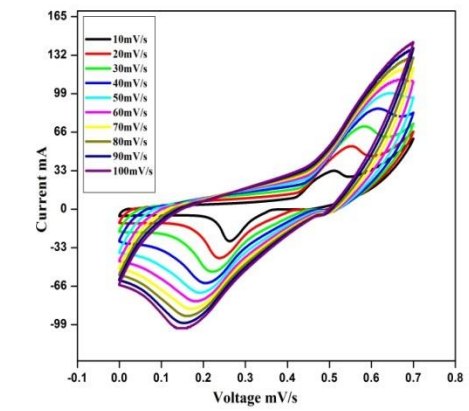

(c)

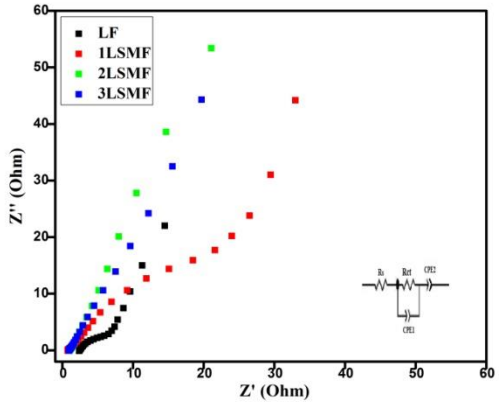

(d)

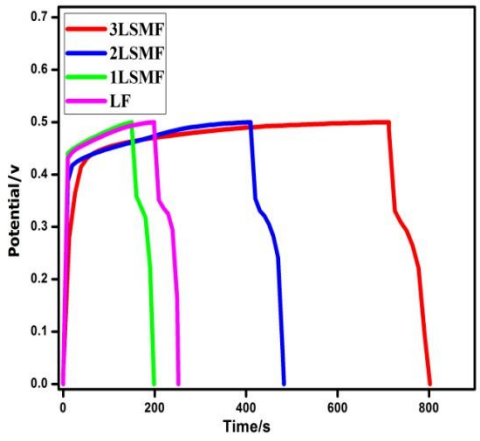

(e)

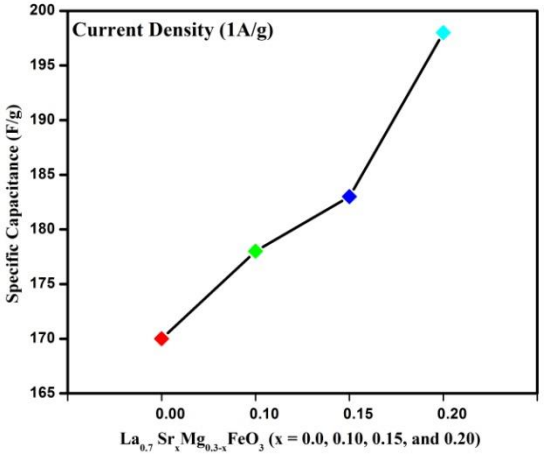

(f)

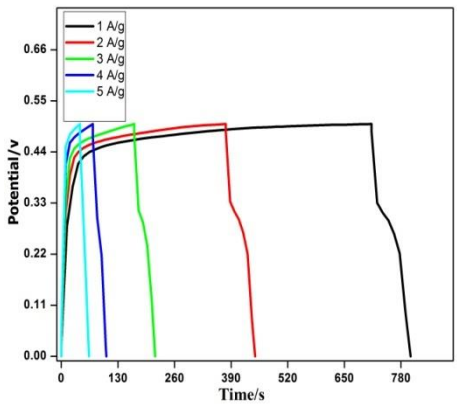

(g)

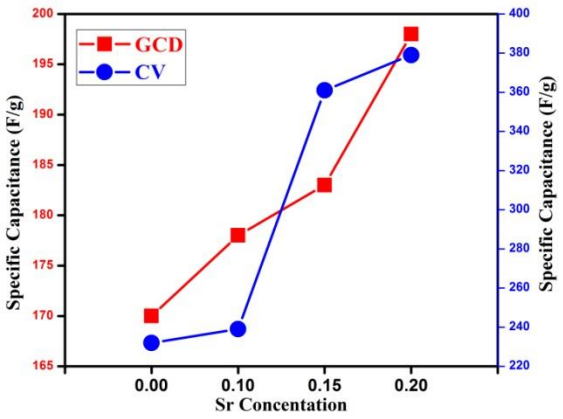

(h)

Fig. 8. CV analysis plots (color online)

It could be attributed to the fact that Sr and Mg nanoclusters included LSMF nanoparticles, which facilitated ionic transport at the electrode/electrolyte interface and decreased the diffusion resistance of the synthesised nanocomposite samples To be more precise, the charge transfer resistance reduces in the nanocomposite in the following order: LF > 1LSMF > 2LSMF > 3LSMF. High specific capacitance is produced by the current collector because to the Sr and Mg's strong electronic conductivity, which also acts like a conducting network that operates for quick electron transfer between LSMF nanoparticles. The two primary causes of this phenomenon

are (i) the tiny form of LSMF nanoparticles, which results in a short electron pathway, and (ii) the minimal interfacial resistance in the charge transfer process, which is caused by well-dispersed LSMF nanoparticles that are in close association with extremely conducting nanoclusters [47, 49].

Fig. 8 (e) shows the GCD curves for the pure LF and LSMF samples at various current densities between 1 and 5 A/g. The samples' greatest discharge times at 1 A/g current densities suggest that materials that have been prepared perform better electrochemically effectively at low current densities. Based on the GCD test, the samples' Cp values were assessed using:

$$C_p = \frac{I\Delta t}{m\Delta V} \quad (3)$$

where I is the charging and discharging current density in A/g, V is the potential window of GCD performance which measured in volts (V), and t is the discharge duration in seconds (s) [50]. The calculated Cp values for the LF, 1LSMF, 2LSMF, and 3LSMF samples are 170, 178, 183, and 198 F/g, respectively. Fig. 8 (f) illustrates the comparison of the GCD curves for the nanocomposite samples of LF, 1LSMF, 2LSMF, and 3LSMF. Fig. 8 (g) represents the curve of a single nanocomposite 3LSMF sample. The 3LSMF nanocomposite has a long charging time and a high specific capacitance when compared to other nanocomposites.

4. Conclusion

The sol-gel citrate self-igniting process has been used to synthesize $La_{0.7}Sr_xMg_{0.3-x}FeO_3$ nanoparticles (x = 0.0, 0.10, 0.15, and 0.20). The $LaFeO_3$ molecule retains its orthorhombic structure, and structural analysis (XRD) has revealed that their space group remains Pnma (62). The estimated range of the average crystallite size (Dc) is 21 to 28 nm. The band gap (E_g) has been calculated using Tauc's figure, and its values slightly varies in the range of 2.08 eV to 2.13 eV depending on the dopants. In addition, significant peaks at 570 and 470 cm^{-1} have been linked to vibrations of O-Fe-O deformation and Fe-O stretching, respectively, which support the sample's ferrite behaviour. The SEM images clearly illustrate the porous, non-spherical (coral-like) shape, and the EDX spectra provided additional evidence of the presence of the appropriate doping materials in the lanthanum ferrite. Pure lanthanum ferrite exhibits paramagnetism from the M-H loop. The magnetic phase changed from paramagnetic to ferromagnetic when Sr and Mg were added at concentrations (x = 0.10, 0.15, and 0.20). The synthesised Sr and Mg incorporated samples, which have been determined to have coercivity values of 115Oe, 152Oe and 185 Oe, may be effectively utilized in magnetic recording, data storage devices, etc. As a result, Sr and Mg-doped perovskite $LaFeO_3$ nanoparticles might be considered a potentially useful material for multiferroic applications. CV results show that the specific capacitance of lanthanum ferrite can be increased by adding Sr and Mg to pure perovskite samples. At a scan rate of 10 mV/s, the specific capacitance (Cs) of LF is 233 F/g. Intriguingly, as compared to pure LF and 3LSMF, the composites of $La_{0.7}Sr_xMg_{0.3-x}FeO_3$ (x =0.20) showed a significantly higher specific capacitance. The 3LSMF nanocomposite's specific capacitance was 379 F/g at10 mV/s.

Acknowledgements

1. I, S.Saseetha (Reg.No: 19222232132014) is thankful to authorities of V. O. Chidambaram College, Thoothukudi and Manonmaniam Sundaranar University, Tirunelveli, Tamilnadu, India for providing necessary research facilities.

References

[1] D. Sari Hasnah, M. Ade, S. Yosef, S. W. Didin, A. A. Wisnu, J. Rare Earths **41**(4), 578 (2023).
[2] F. Bi, R. Liu, G. Gai, X. Dong, J. Optoelectron. Adv. M. **25**(3-4), 150 (2023).
[3] Y. Fu, Y. Wan, H. Xia, X. Wang, J. Power Sources **213**, 338 (2012).
[4] J. Dantas, E. Leal, A. B. Mapossa, D. R. Cornejo, A. C. F. M. Costa, Fuel **191**, 463 (2017).
[5] A. B. Gadkari, T. J. Shinde, P. N. Vasambekar, J. Alloys Compd. **509**(3), 966 (2011).
[6] K. Lin, A. K. Adhikari, Z. Tsai, Y. Chen, T. Chien, H. Tsai, Catal. Today **174**(1), 88 (2011).
[7] V. S. Kumbhar, A. D. Jagadale, N. M. Shinde, C. D. Lokhande, Appl. Surf. Sci. **259**, 39 (2012).
[8] A. Muhammad, H. G. Iftikhar, N. Khalid, Y. Khurram, J. Rare Earths **37**(2), 193 (2019).
[9] W. Haron, A. Wisitsoraat, S. Wongnawa, Ceram. Int. **43**(5), 5032 (2017).
[10] A. Kumar, S. Kumar, A. Bahuguna, A. Kumar, V. Sharma, V. Krishnan, Mater. Chem. Front. **1**, 2391(2017).
[11] M. Kaltenbrunner, G. Adam, E. D. Głowacki, M. Drack, R. Schwödiauer, L. Leonat, D. H. Apaydin, H. Groiss, M. C. Scharber, M. S. White, N. S. Sariciftci, S. Bauer, Nat. Mater. **14**(10), 1032 (2015).
[12] W. Zhou, R. Ran, Z. P. Shao, J. Power Sources **192**(2), 231 (2009).
[13] J. H. Kim, P. W. Liang, S. T. Williams, N. Cho, C. C. Chueh, M. S. Glaz, D. S. Ginger, A. K. Y. Jen, Adv. Mater. **27**(4), 965 (2015).
[14] C. Pan, T. Takata, M. Nakabayashi, T. Matsumoto, N. Shibata, Y. Ikuhara, K. Domen, Angew. Chem. Int. Ed. **54**(10). 2955 (2015).
[15] W. Wang, M. O. Tade, Z. P. Shao, Chem. Soc. Rev. **44**, 5371 (2015).
[16] E. Grabowska, Appl. Catal. B. **186**, 97 (2016).
[17] K. R. Phillips, G. T. England, S. Sunny, E. Shirman, T. Shirman, N. Vogel, J. Aizenberg, Chem. Soc. Rev. **45**, 281 (2016).
[18] E. Cao, Y. Yang, T. Cui, Y. Zhang, W. Hao,

L. Sun, H. Peng, X. Deng, Appl. Surf. Sci. **393**, 134 (2017).
[19] W. Wei, S. Guo, C. Chen, L. Sun, Y. Chen, W. Guo, S. Ruan, J. Alloys Compd. **695**, 1122 (2017).
[20] M. I. A. Abdel Maksoud, A. El-Ghandour, A. H. Ashour, M. M. Atta, S. Abdelhaleem, A. H. El-Hanbaly, R. A. Fahim, S. M. Kassem, M. S. Shalaby, A. S. Awed, J. Rare Earths **39**(1), 75 (2012).
[22] R. Hirian, S. Mican, O. Isnard, V. Pop, J. Optoelectron. Adv. M. **24**(11-12), 594 (2022).
[23] J. Luo, R. Li, Y. Chen, X. Zhou, X. Ning, L. Zhan, L. Ma, X. Xu, L. Xu, L. Zhang, Sep. Purif. Technol. **210**, 417 (2019).
[24] F. Bidrawn, S. Lee, J. M. Vohs, R. J. Gorte, J. Electrochem. Soc. **155**, 660 (2008).
[25] J. M. Liu, Q. C. Li, X. S. Gao, Y. Yang, X. H. Zhou, X. Y. Chen, Z. G. Liu, Phys. Rev. B. Condens. Matter. **66,** 54416 (2002).
[26] X. Dai, G. Yu, R. Li, Q. Wu, K. Shi, Z. Hao, J. Rare Earths **26**(3), 341 (2008).
[27] M. Zhao, J. Liu, J. Liu, J. Xu, Z. Zhao, Y. Wei, W. Song, J. Rare Earths **38**(4), 369 (2020).
[28] N. Elgrishi, K. J. Rountree, B. D. McCarthy, E. S. Rountree, T. T. Eisenhart, J. L. Dempsey, J. Chem. Educ. **95**(2), 197 (2018).
[29] E. P. Karadeniz, A. N. Grundy, M. Chen, T. Ivas, L. J. Gauckler, J. Phase Equilib. Diffus. **30**, 351 (2009).
[30] Q. Liu, Z. You, S. J. Zeng, H. Guo, J. Sol-Gel Sci. Technol. **80**, 860 (2016).
[31] M. B. Bellakki, V. Manivannan, J. Das, Mater. Res. Bull. **44**, 1522 (2009).
[32] A. Hajalilou, S. A. Mazlan, S. T. Shila, Mater. Lett. **181**, 196 (2016).
[33] F. Kashanian, M. Habibi-Rezaei, A. R. Bagherpour, A. Seyedarabi, A. A. Moosavi-Movahedi, RSC Adv. **7l**, 54813 (2017).
[34] Z. Kaiwen, W. Xuehang, W. Wenwei, X. Jun, T. Siqi, L. Sen, Adv. Powder Technol. **24**, 359(2013).
[35] R. Anitha, E. Kumar, S. C. Vella Durai, M. Vargheese, J. Optoelectron. Adv. M. **23**(11-12), 598 (2021).
[36] F. T. Thema, E. Manikandan, A. Gurib-Fakim, M. Maaza, J. Alloys Compd. **657**, 655 (2016).
[37] A. A. Saad, W. Khan, P. Dhiman, A. H. Naqvi, M. Singh, Electron. Mater. Lett. **9**, 77 (2013).
[38] J. Kennedy, P. P. Murmu, J. Leveneur, A. Markwitz, J. Futter, Appl. Surf. Sci. **367**, 52 (2016).
[39] S. Rahman, K. Nadeem, M A. Rehman, M. Mumtaz, S. Naeem, I. L. Papst, Ceram. Int. **39**, 5235 (2013).
[40] Q. Lin, J. Lin, X. Yang, Y. He, L. Wang, J. Dong, Ceram. Int. **45**(3), 3333 (2019).
[41] A. Rai, A. K. Thakur, Ceram. Int. **43**(16), 13828 (2017).
[42] J. Li, X. Kou, Y. Qin, H. He, J. Appl. Phys. **92**(12), 7504 (2002).
[43] A. Rezanezhad, E. Rezaie, L. S. Ghadimi, A. Hajalilou, E. Abouzari-Lotf, N. Arsalani, Electrochim. Acta **335**, 135699 (2020).
[44] Y. Cao, B. Lin, Y. Sun, H. Yang, X. Zhang, J. Alloys Compd. **624**, 31 (2015).
[45] P. Xiong, C. Hu, Y. Fan, W. Zhang, J. Zhu, X. Wang, J. Power Sources **266**, 384 (2014).
[46] A. Rai, A. K. Thakur, Ionics **23**, 2863 (2017).
[47] H. S. Nan, X. Y. Hu, H. W. Tian, Mater. Sci. Semicond. Process **94**, 35 (2019).
[48] C. Xiang, M. Li, M. Zhi, A. Manivannan, N. Wu, J. Power Sources **226**, 65 (2013).
[49] A. V. Ivanishchev, I. A. Bobrikov, I. A. Ivanishcheva, O. Y. Ivanshina, J. Electroanal. Chem. **821**, 140 (2018).
[50] Y. Liu, H. Huang, X. Peng, Electrochim. Acta **104**, 289 (2013).
[51] A. Mohammadi, N. Arsalani, A. G. Tabrizi, S. E. Moosavifard, Z. Naqshbandi, L. S. Ghadimi, Chem. Eng. J. **334**, 66 (2018).

*Corresponding author: sasiathi1@gmail.com